PNAS
www.pnas.org

Supplementary Information for

Multiscale Porous Elastomer Substrates for Multifunctional On-Skin Electronics with Passive-Cooling Capabilities

Yadong Xu[a,1], Bohan Sun[b,1], Yun Ling[b,1], Qihui Fei[a], Zanyu Chen[a], Xiaopeng Li[b], Peijun Guo[c], Nari Jeon[c], Shivam Goswami[b], Yixuan Liao[a], Shinghua Ding[a], Qingsong Yu[b], Jian Lin[b], Guoliang Huang[b,2], Zheng Yan[a,b,2]

[a]Department of Biomedical, Biological & Chemical Engineering, University of Missouri, Columbia, Missouri 65211, USA

[b]Department of Mechanical & Aerospace Engineering, University of Missouri, Columbia, Missouri 65211, USA

[c]Materials Science Division and Center for Nanoscale Materials, Argonne National Laboratory, 9700 South Cass Avenue, Lemont, Illinois 60439, USA

[1]These authors contributed equally to this work.

[2]Corresponding author. E-mail: yanzheng@missouri.edu; huangg@missouri.edu

www.pnas.org/cgi/doi/10.1073/pnas.1917762116

This PDF file includes:

Movie S2. EMGs recording in water.
Movie S3. Interactive virtual reality.
Movie S4. Real-time control of a drone quadcopter.

Note S1: Calculations of hemispherical solar reflectance and thermal emittance of the multiscale porous SEBS substrate

To efficiently scatter and reflect sunlight at all wavelength, the porous SEBS substrate needs to have high angular solar reflectance $\bar{R}_{solar}(\theta)$, defined as:

$$\bar{R}_{solar}(\theta) = \frac{\int_0^\infty I_{solar}(\lambda) R_{solar}(\theta,\lambda) d\lambda}{\int_0^\infty I_{solar}(\lambda) d\lambda}$$

where θ is the angle between incidence angle and surface normal, λ is wavelength, $I_{solar}(\lambda)$ is the ASTM G173 Global solar intensity spectrum, and $R_{solar}(\theta,\lambda)$ is the surface's angular reflectance. As the solar reflectance of the randomly oriented, porous structures are demonstrated to be almost independent on angles (*1*), thus $\bar{R}_{solar}(\theta,\lambda)$ and $\bar{R}_{solar}(\lambda)$ is regarded as the same.

To maximize heat dissipation from human body to the environment, the SEBS substrate needs to have high IR thermal emittance $\bar{\epsilon}_{HB}$ over the range where human body emits heat energy, defined as:

$$\bar{\epsilon}_{HB} = \frac{\int_{7\mu m}^{14\mu m} I_{BB}(T,\lambda)\epsilon(T,\lambda) d\lambda}{\int_{7\mu m}^{14\mu m} I_{BB}(T,\lambda) d\lambda}$$

where the 7-14 μm bounds represent the main range of human body heat radiation, $I_{BB}(T,\lambda)$ is the spectral intensity emitted by a blackbody at temperature T (25 °C) and $\epsilon(T,\lambda)$ is the surface's spectral hemispherical thermal emittance. $I_{BB}(T,\lambda)$ is defined as:

$$I_{BB}(T,\lambda) = \frac{2hc^2}{\lambda^5} \frac{1}{e^{hc/(\lambda k_B T)} - 1}$$

Where h is Planck's constant, k_B is the Boltzmann constant, c is the speed of light.

Note S2: Recycling process

To recycle the on-skin electronic patch based on porous SEBS substrates and spray-printed Ag NWs, we first dissolved the on-skin electronic patch in chloroform to make a SEBS solution (~60 mg/ml) containing a small amount of Ag NWs. The resulting solution was then subject to centrifugation at 4,000 rpm for 10 mins to separate Ag NWs from the solution. The supernatant was then collected and mixed with isopropyl alcohol at a volume ratio of 5:2 for the subsequent phase-separation-controlled synthesis of the SEBS substrates with multiscale porous structures. The collected Ag NWs segments were washed with chloroform and ethanol each for three times to remove the SEBS residuals, and were subsequently dispersed in ethanol by sonication. The recycled Ag NWs solution were then spray-printed onto porous SEBS substrates, which were made of the recycled SEBS, to pattern the bioelectronic devices mentioned in the maintext.

Note S3: Correlation between blood pressure and pulse transit time (PTT)

Blood pressure is correlated with the elastic modulus of the blood vessel, determined by Hughes equation:

$$\mathrm{E} = E_0 e^{\alpha P}$$

where α is 0.017 $mmHg^{-1}$ and P stands for the mean blood pressure. In a short elastic vessel, the PTT is inversely proportional to the pulse wave velocity (PWV), is obtained from geometric and elastic properties of the blood vessel, and is descripted by the Moens–Korteweg equation:

$$\mathrm{PWV} = \frac{distance}{PTT} = \sqrt{\frac{Eh}{\rho 2r}}$$

where h is the thickness of the blood vessel, r is its radius, and ρ is the density of blood. Based on the equation above, assuming constant vessel thickness and radius, mean blood pressure is correlated with PTT according to a logarithmic relation: $\mathrm{P} = \mathrm{kln(PTT)} + \mathrm{b}$.

Systolic blood pressure (SDP) and diastolic blood pressure (DBP) are correlated with PTT, as follows:

$$\mathrm{DBP} = \frac{SBP_0}{3} + \frac{2DBP_0}{3} + Aln\left(\frac{PTT_0}{PTT}\right) - \frac{(SBP_0 - DBP_0)}{3}\frac{PTT_0^2}{PTT^2}$$

$$\mathrm{SBP} = \mathrm{DBP} + (\mathrm{SB}P_0 - DBP_0)\frac{PTT_0^2}{PTT^2}$$

where SBP_0 and DBP_0 are determined by a commercial sphygmomanometer from a one-time calibration, A is a subject-dependent coefficient yet can be estimated for the population, and PTT_0 is the initial PTT of the first recorded cycle.

Note S4: EMG signals classification and processing

The classification of four individual commands was based on two-channel EMG signals generated by contraction of the flexor carpi radialis muscles of the left and right forearms of a volunteer. Four commands can be generated with the combination of two gestures (bends the wrist to outward and inward) in each forearm. EMG signals measured by PowerLab T26 were streamed to MATLAB (The Mathworks, Inc., Natick, MA) for simultaneous sampling analysis. EMG signals obtained during bimanual gestures were converted to root-mean-square (RMS) values with a moving window of 400 ms for extraction and real-time classification. The RMS is described as:

$$\mathrm{RMS} = \sqrt{\frac{1}{N}\sum_{k=1}^{N}[x_k]^2}$$

where N is the number of samples and x_k is the k^{th} sample. A trial test was carried out to determine the baseline, which was the maximum RMS value after the resting of forearms for 10 s. The null state was therefore defined as an RMS value below the baseline.

RMS values from each channel were divided into one category (1) for soft robotic hand control and two categories (1 and 2) for virtual reality and human machine interface applications except null state due to their characteristic motion-dependent feature, and thus can be used to control the smart switch in the robotic hand control and four commands (A, B, C and D) in the virtual reality and quadcopter control with the two-channel EMG signals. As a priori examination, a training session where participants repeated each gesture 10 times was used to determine a conservative threshold, which can largely improve the accuracy and reliability of the electronic device.

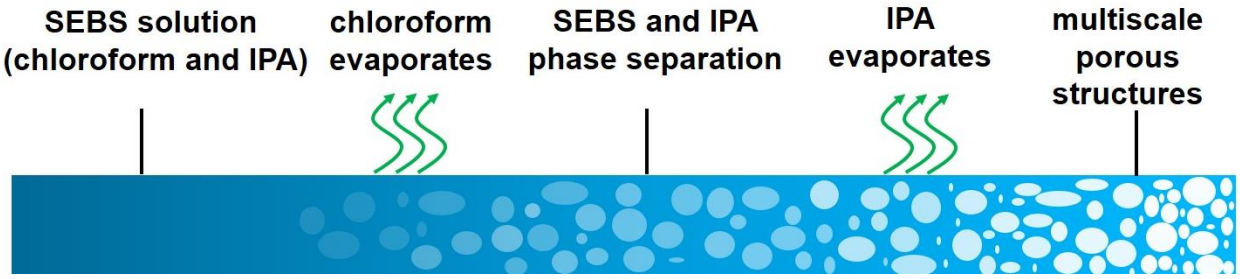

Fig. S1. Schematic illustrations of the formation process of the SEBS substrates with hierarchical pores through a phase-separation-controlled method. Here, chloroform and IPA serve as solvent and nonsolvent, respectively.

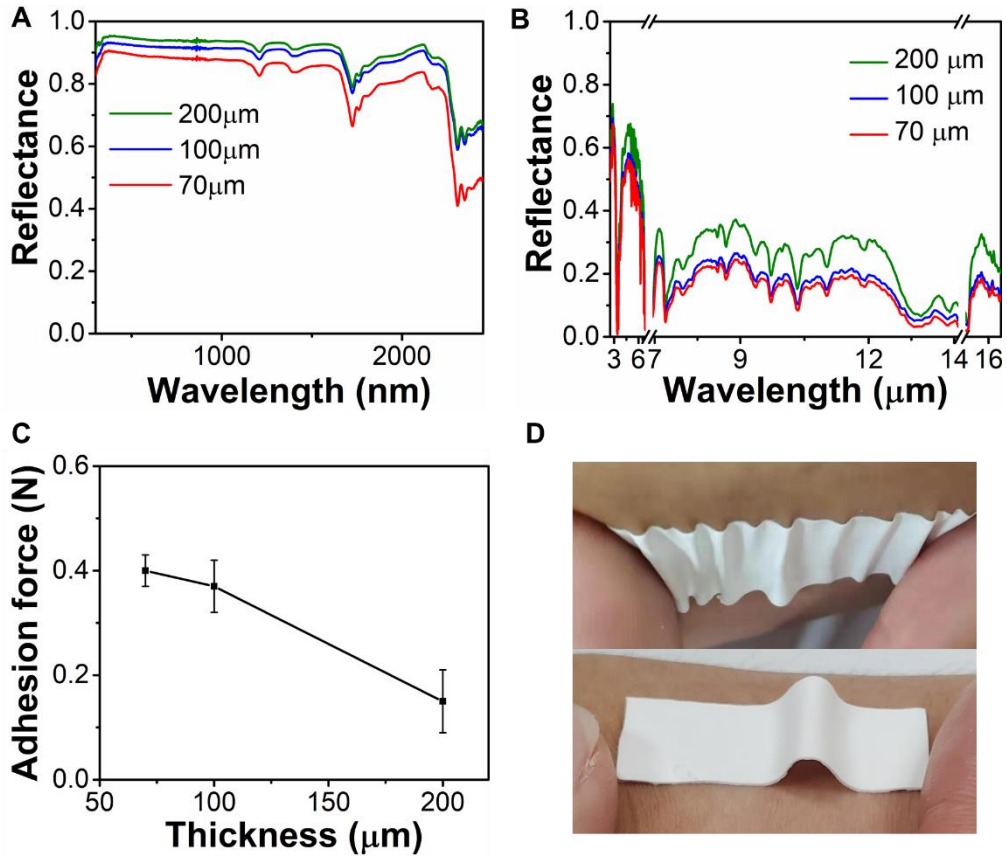

Fig. S2. Thickness optimization of porous SEBS substrates based on sunlight reflectance, mid-IR reflectance, and conformability with human skin. The solar radiation reflectance **(A),** mid-IR radiation reflectance **(B)** and skin adhesion forces **(C)** of the porous SEBS substrates with the thicknesses of ~70 μm, ~100 μm and ~200 μm. The error bars in **(C)** are based on three individual measurements. **(D)** Optical images, indicating that the porous SEBS substrates with the thicknesses of ~140 μm (top) and ~200 μm (bottom) can easily delaminate from skin under compression. Thus, in this research, the optimal thickness (~100 μm thick) of porous SEBS was adopted for the fabrication of on-skin electronic devices based on the tradeoff of sunlight reflectance, mid-IR reflectance, and conformability with human skin.

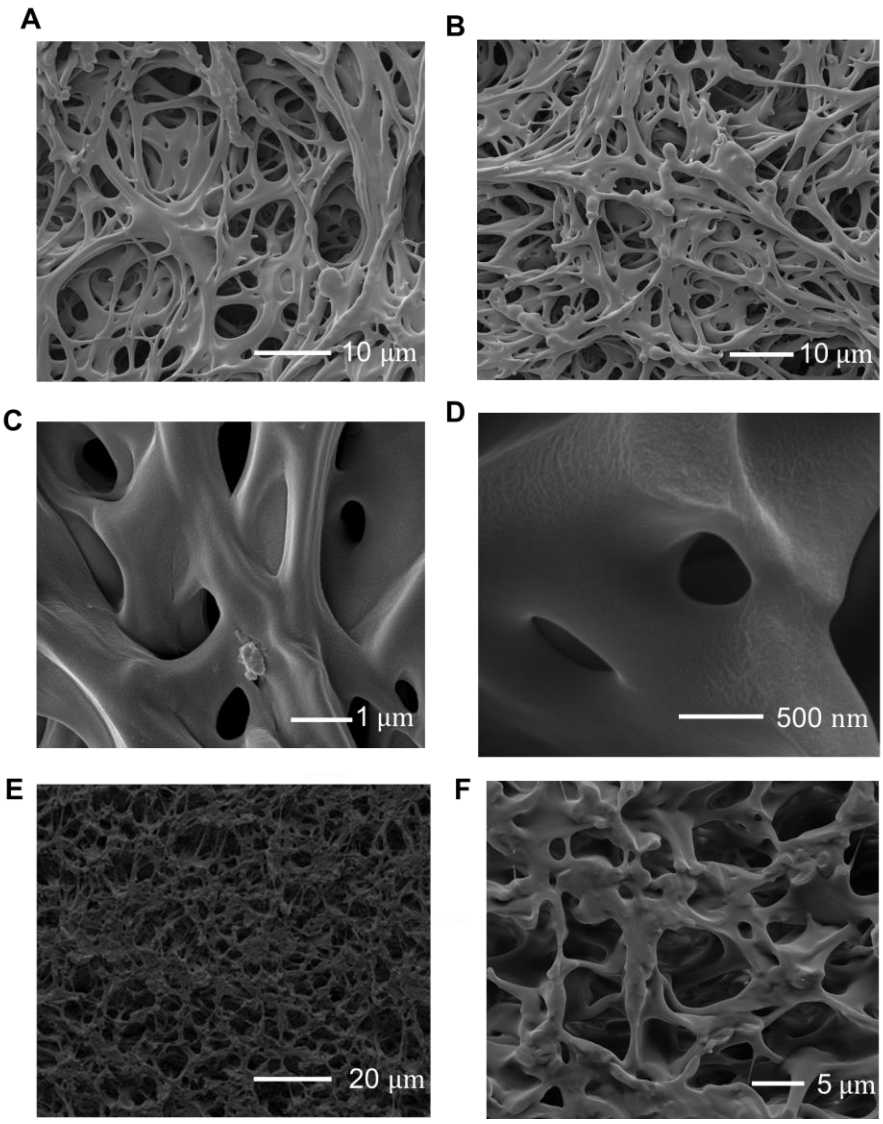

Fig. S3. SEM images of the SEBS substrates with multiscale porous structures. (A-D) SEM images of the top view with different magnifications. (**E, F**) SEM images of cross-section view with different magnifications. SEM images show that the obtained SEBS substrates exhibit interconnected, hierarchical pores and a large amount of nanopores are embedded in the walls of micropores.

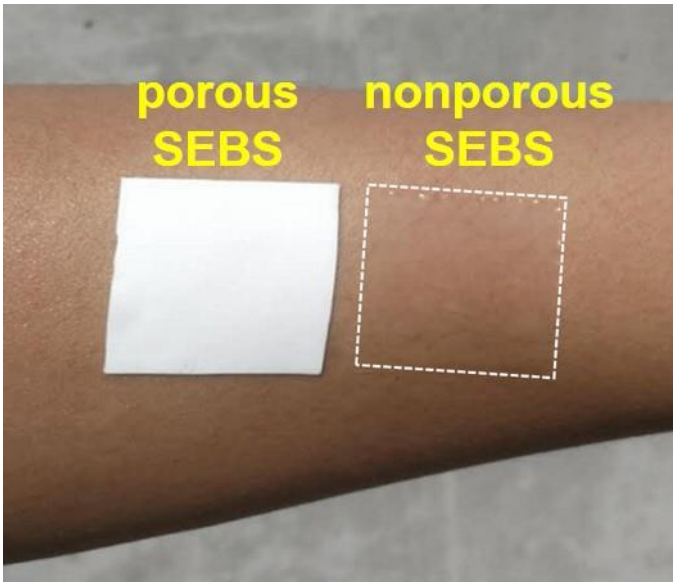

Fig. S4. A photograph of porous SEBS (white) and nonporous SEBS (transparent) with same thickness attached onto the forearm of a human volunteer, corresponding to the IR thermal image shown in Fig. 1F.

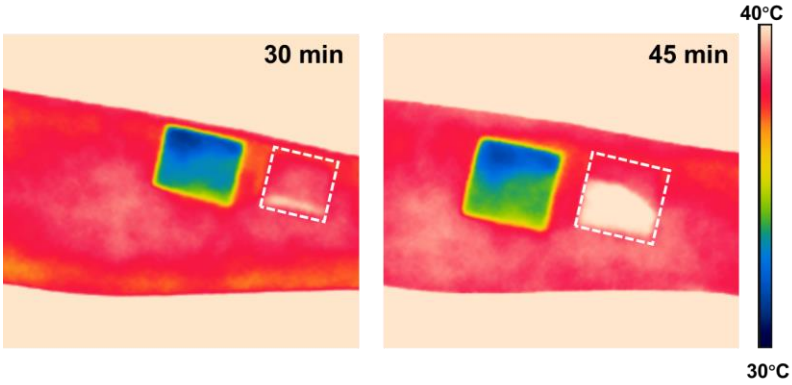

Fig. S5. Thermal mapping images of porous and nonporous SEBS substrates on the human forearm after 30 and 45 mins of sunlight radiation under the solar intensity of ~840 W m^{-2}. With the increased exposed time of sunlight radiation, the skin temperature covered with porous SEBS is maintained at ~6°C lower than that of the exposed skin and ~7°C lower than that of the skin covered with nonporous SEBS with the same thickness.

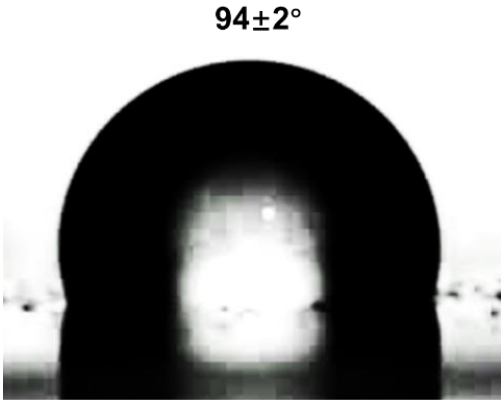

Fig. S6. Water contact angle measurement of nonporous SEBS, showing around 31° lower than that of porous SEBS. The enhanced hydrophobicity can be attributed to significantly increased surface roughness stemming from the porous structures. On a rough surface, water contact angle can be described with Wenzel equation

$$\cos\theta_m = r\cos\theta_Y,$$

where θ_m is the measured contact angle, θ_Y is the Young contact angle (for ideal smooth surface), and r is the roughness ratio. Accordingly, the hydrophobic surface becomes more hydrophobic as surface roughness increases.

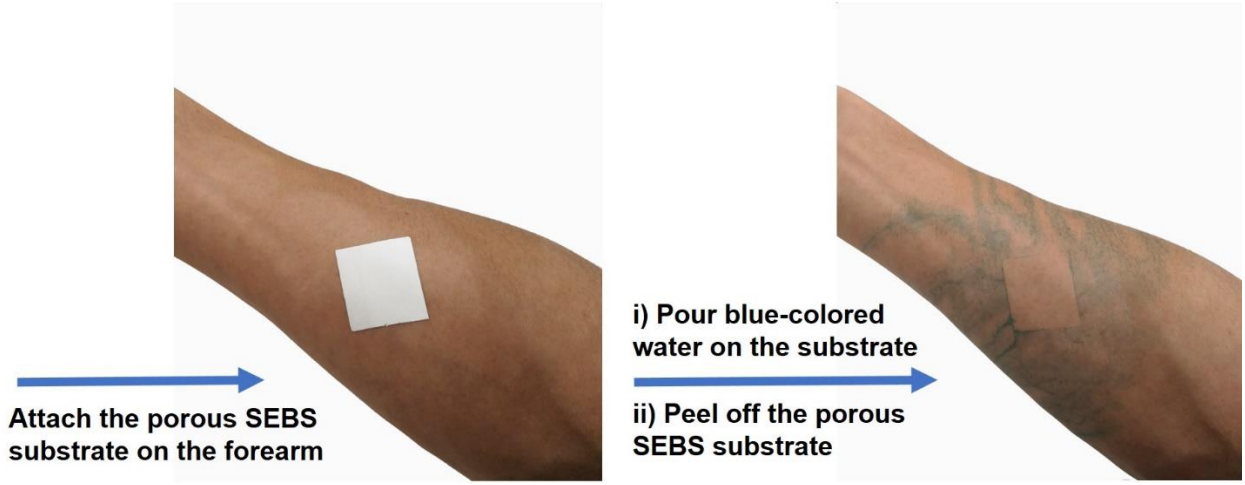

Fig. S7. Waterproof test. A porous SEBS substrate was attached onto the forearm of a human volunteer. Then, the blue-colored water was poured onto the substrate. Water did not penetrate into the skin area covered by the porous SEBS substrate, indicating its outstanding waterproof capability, largely because of its high hydrophobicity and conformal contact with the skin.

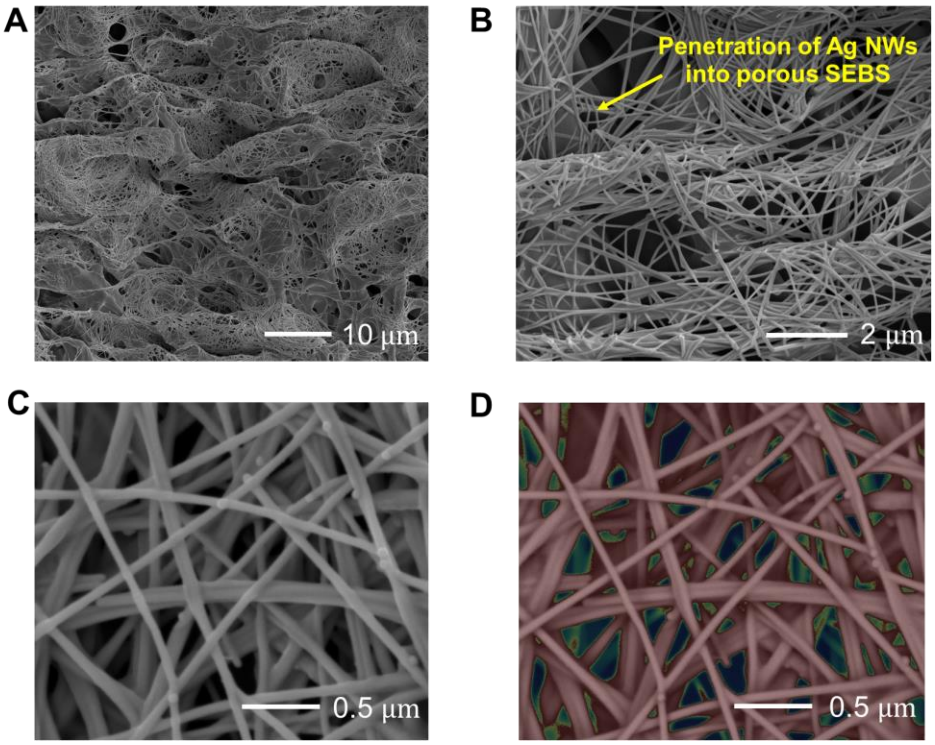

Fig. S8. SEM images of spray-printed Ag NWs on porous SEBS. (A, B) SEM images of spray-printed Ag NWs on porous SEBS, indicating the formation of microscale wavy structures as well as strong bonding interface because of the penetration of Ag NWs into the pores. The robust interfacial adhesion is further confirmed via the cycling bending and stretching tests (Fig. S7). The high-magnification SEM image of Ag NWs networks **(C)** and the corresponding simulated SEM image with Wolfram Mathematica **(D)**, which are used for the estimation of the thickness, surface coverage and porosity of the spray-printed Ag NWs networks.

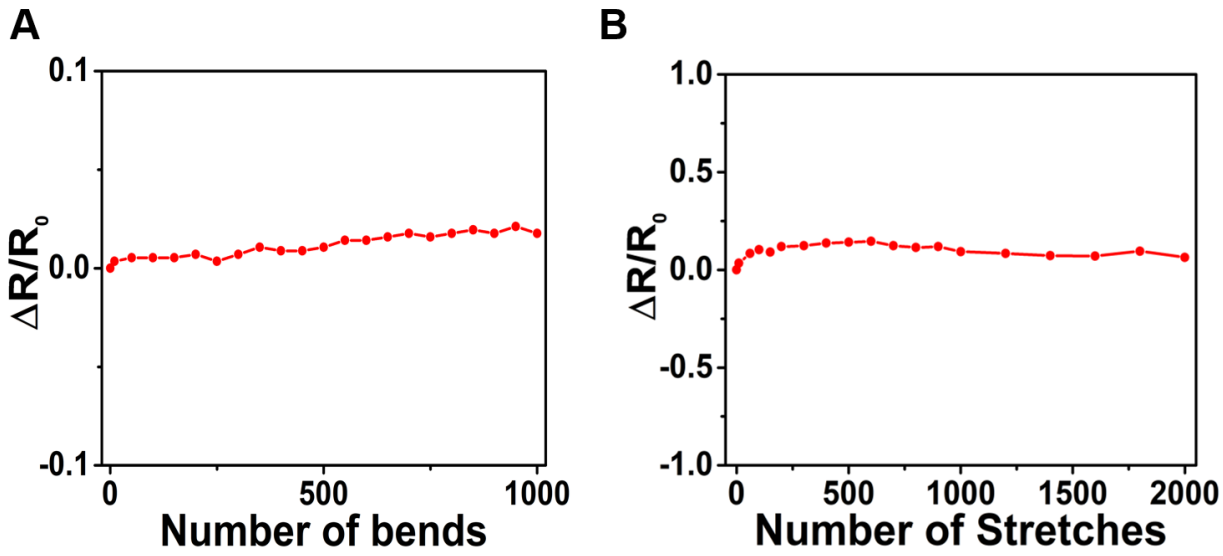

Fig. S9. Normalized electrical resistance changes under the cycling bending and stretching tests. (**A**) 1,000 cycles of bending test under the bending radius of 1 mm. (**B**) 2,000 cycles of stretching test under the uniaxial strain of 50%. Notably, after 1,000 cycles for a bending radius of 1 mm, the resistance only increases ~1.7%. Similarly, only ~6% resistance increase is observed after 2,000 cycles of stretching test under 50% strain.

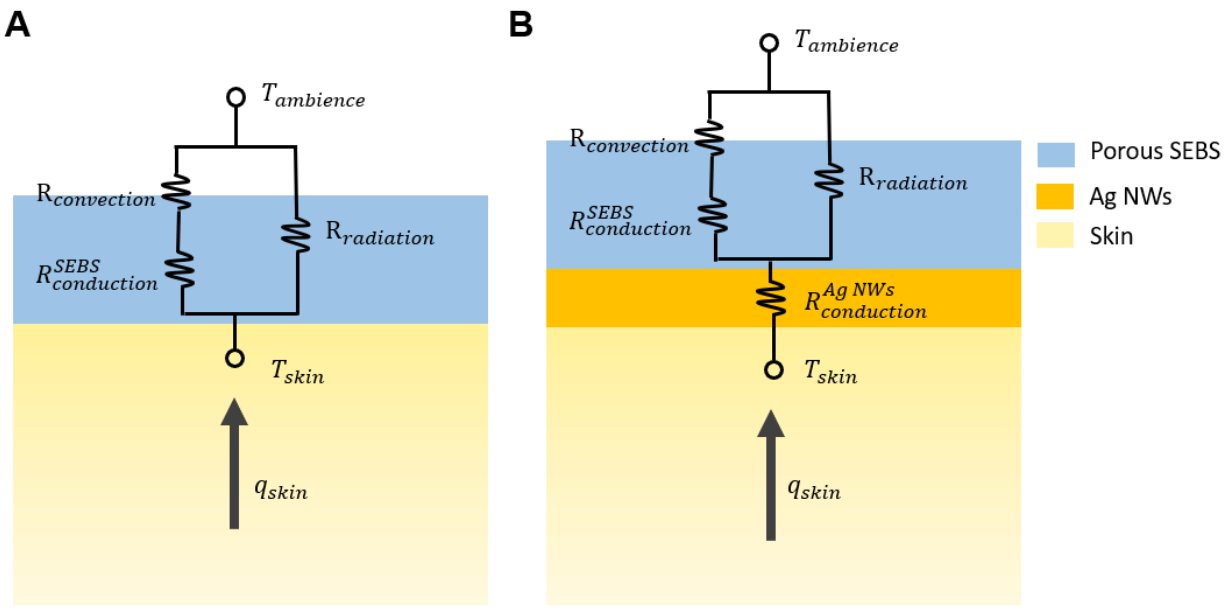

Fig. S10. Thermal circuit model when porous SEBS forms conformal contact with human skin. (A) without Ag NWs. **(B)** with Ag NWs. Since Ag NWs are directly in contact with the skin, they would serve as an ultrathin layer (~200 nm thick) of thermal conductor between porous SEBS and the skin, meaning that the temperature of the former is the same as the latter. The total heat transfer resistance for porous SEBS without Ag NWs from the surface of skin to the outer environment is described as:

$$R^{SEBS}_{total} = \frac{(R_{convection} + R^{SEBS}_{conduction})R_{radiation}}{R_{convection} + R^{SEBS}_{conduction} + R_{radiation}}$$

While for porous SEBS with Ag NWs:

$$R^{SEBS/Ag\ NWs}_{total} = R^{Ag\ NWs}_{conduction} + \frac{(R_{convection} + R^{SEBS}_{conduction})R_{radiation}}{R_{convection} + R^{SEBS}_{conduction} + R_{radiation}}$$

where $R_{convection}$, $R^{SEBS}_{conduction}$, $R_{radiation}$, $R^{Ag\ NWs}_{conduction}$ are heat transfer resistance of air convection, SEBS conduction, SEBS radiation and Ag NWs conduction, respectively.

Due to the low thermal resistance (high thermal conductivity) and ultrasmall thickness (~200 nm) of Ag NWs, R^{SEBS}_{total} and $R^{SEBS/Ag\ NWs}_{total}$ are assumed to be equivalent.

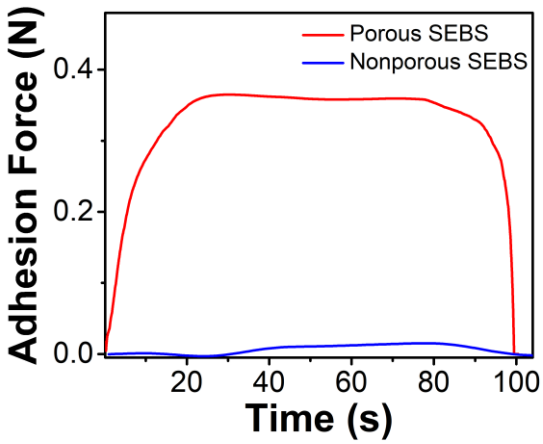

Fig. S11. Peel adhesion test of porous and nonporous SEBS substrates (~100 μm thick) from the human forearm. The sample sizes are around 1.5 cm x 4 cm. After cleaning the skin, alcohol swabs were applied to wet the skin, followed by the lamination of SEBS substrates. The peel test started after 10 mins of skin cleaning to allow alcohol to completely evaporate in open air.

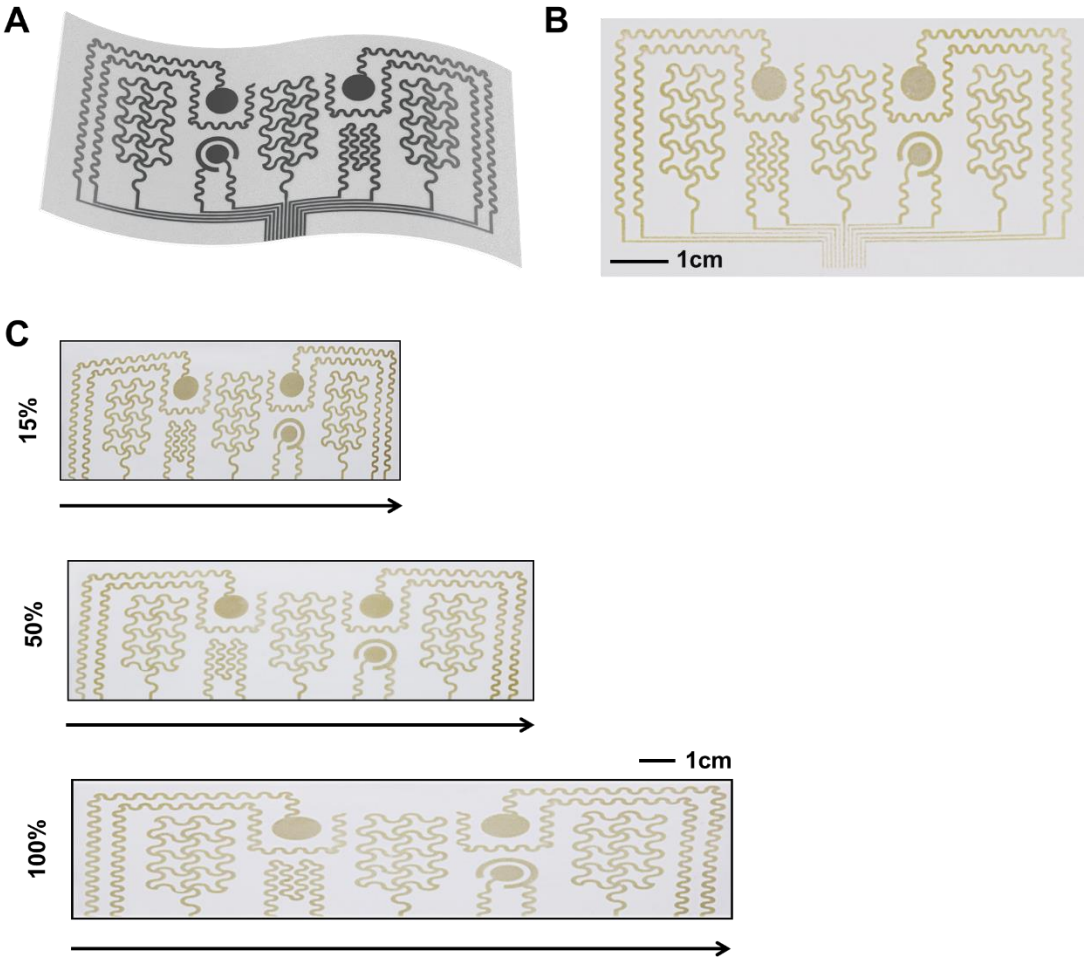

Fig. S12. The obtained multimodal on-skin electronic patch. (A) Schematic. Photographs in the original state **(B)** and under the stretched states with uniaxial strains of 15%, 50% and 100% **(C).** The overall size of the pattern is 7.5 cm × 4 cm, and the line width is ~ 550 μm.

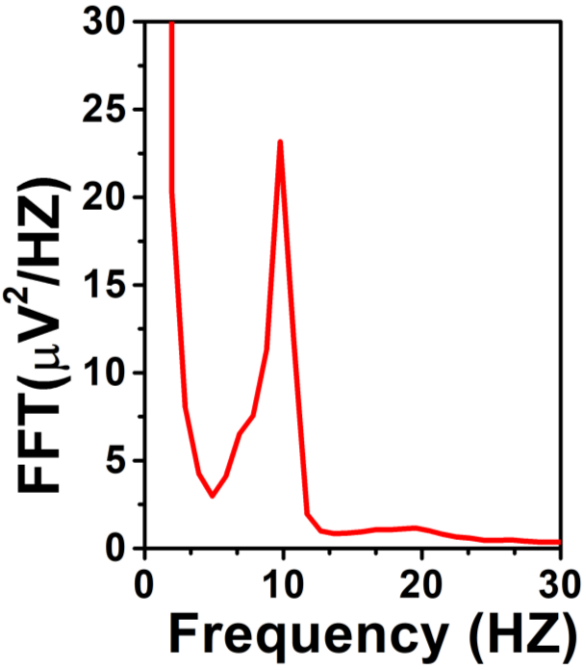

Fig. S13. Fast Fourier transform (FFT) analysis of the electroencephalogram (EEG) signal recorded from the forehead of a volunteer when the volunteer was asked to keep the eyes open for approximately 90 s and then close the eyes for 90 s, showing that the alpha rhythm is centered at ~10 Hz.

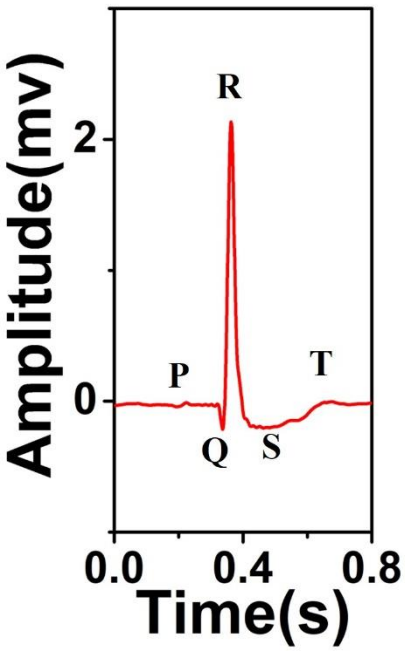

Fig. S14. The magnified ECG signal from Fig. 3B, indicating clearly visible P-wave, QRS complex, and T-wave.

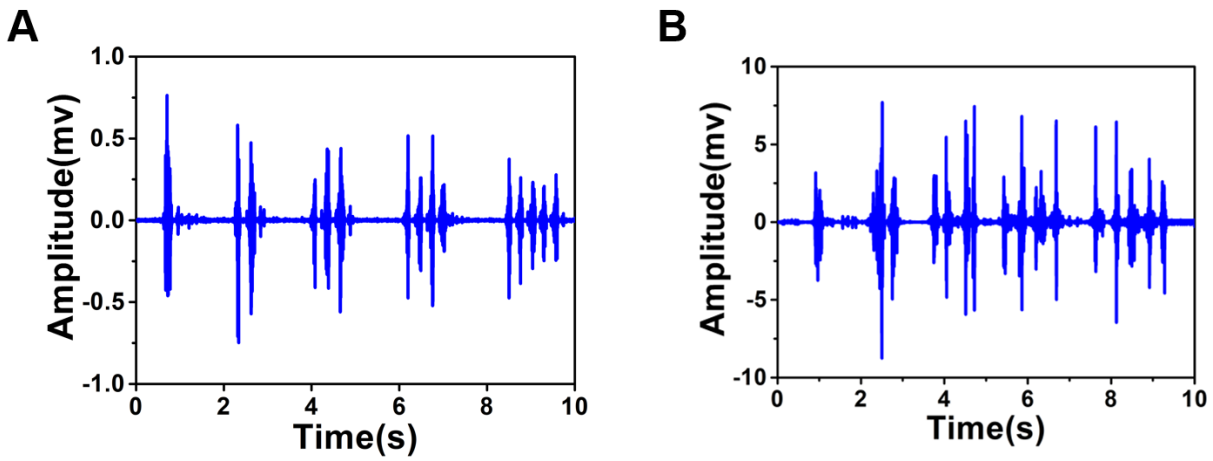

Fig. S15. Recorded EMG signals when the volunteer was asked to clench the jaw (A) and nod the neck (B) for once, twice, three times, four times, and five times. During the testing, the porous on-skin devices were attached onto the volunteer's face (muscle: Masseter) in **A** and back neck (muscle: Trapezius) in **B**, respectively, for EMGs recording.

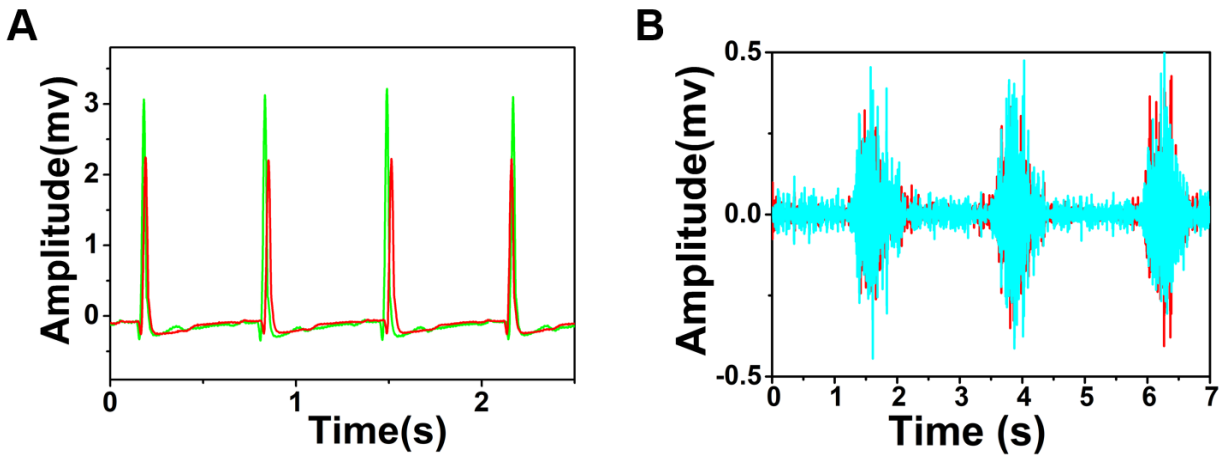

Fig. S16. ECGs and EMGs recorded using the porous on-skin devices (red in A and B; SNR for ECGs: ~22.7 dB; SNR for EMGs: ~20.7 dB) and commercial Ag/AgCl electrodes (green in A and blue in B; SNR for ECGs: ~20.5 dB; SNR for EMGs: ~22.4 dB).

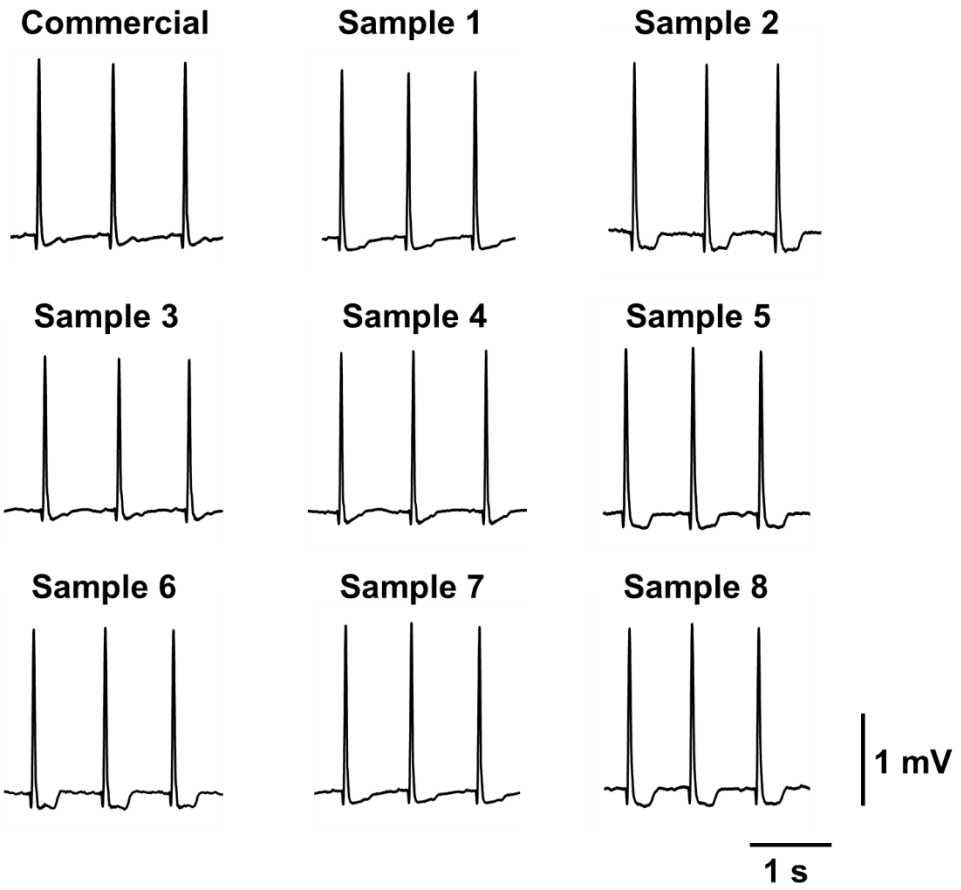

Fig. S17. ECG signals recorded with commercial Ag/AgCl gel electrodes and eight randomly selected porous on-skin devices, demonstrating high reproducibility.

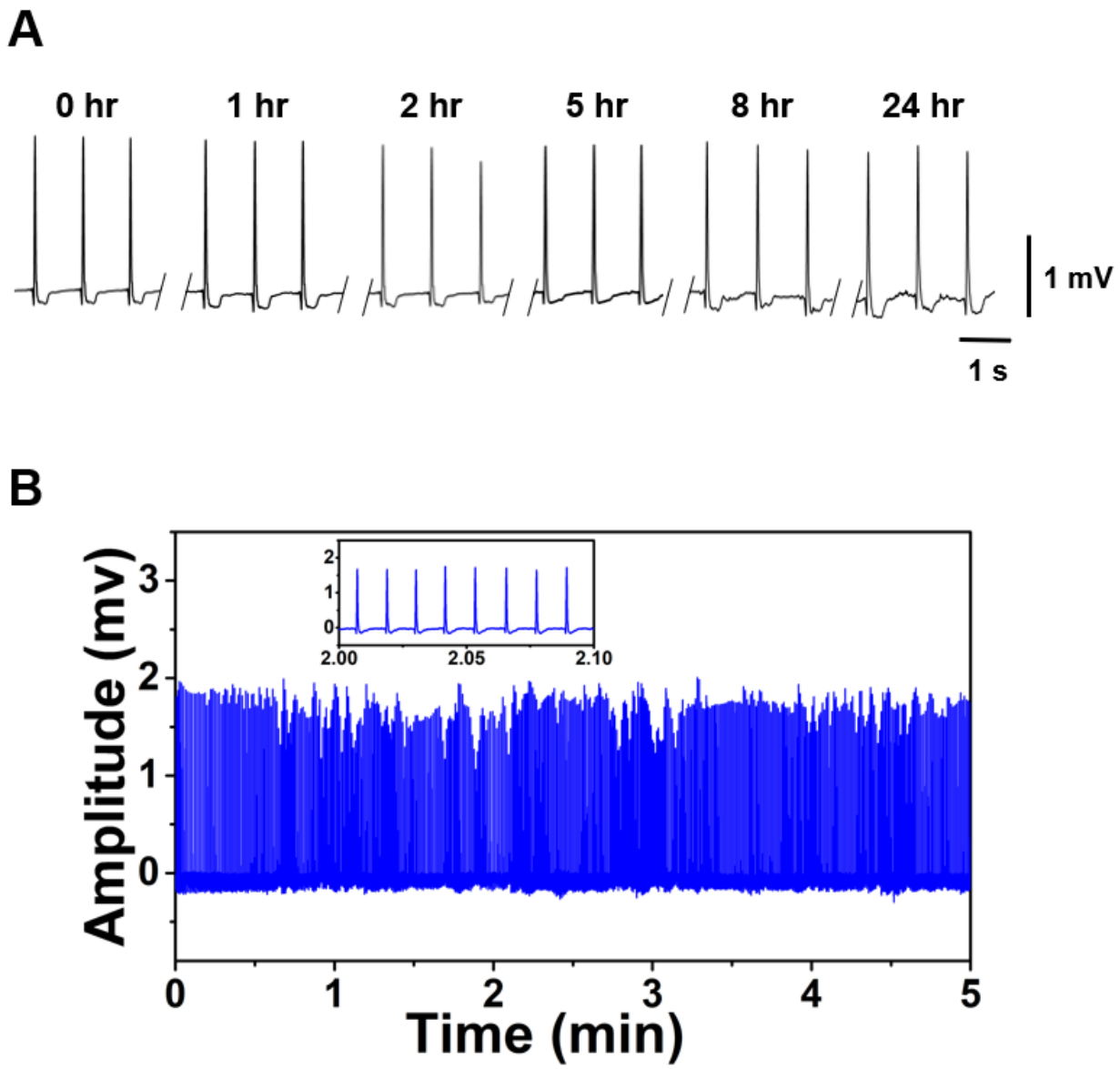

Fig. S18. Long-term and continuous ECGs recording using the porous on-skin device from the chest of a human volunteer, indicating high stability. (**A**) Recorded ECG signals after the volunteer wore the device for 0 h, 1 h, 2 h, 5 h, 8 h, and 24 h. (**B**) Continuous ECGs measurement for 5 min.

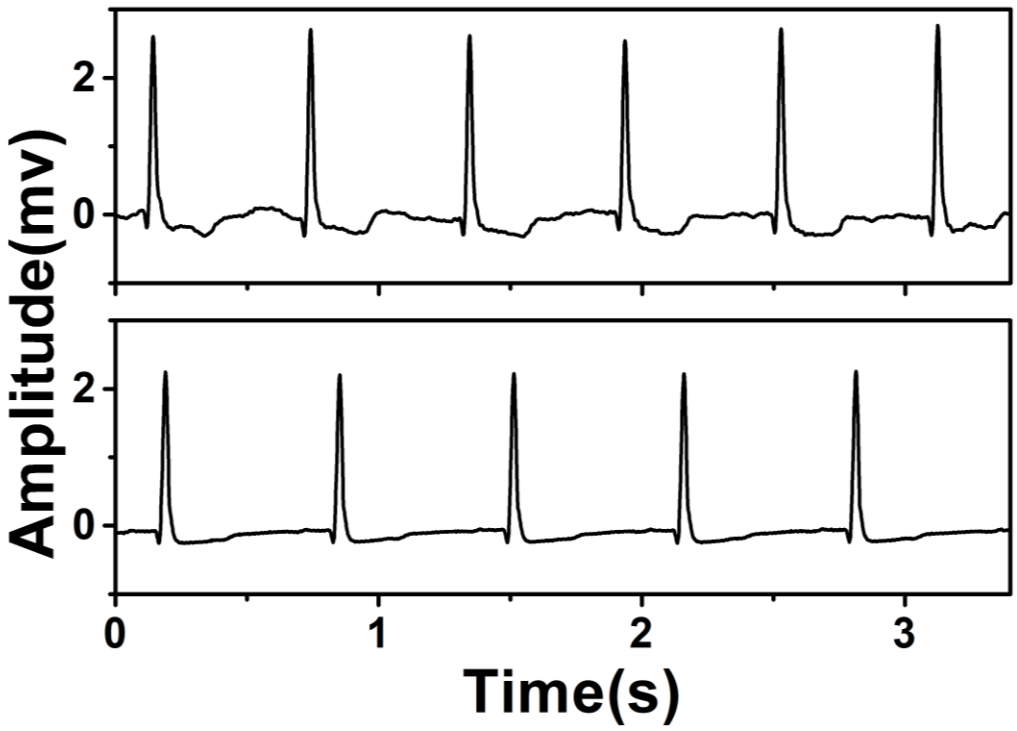

Fig. S19. ECG signals measured by the porous on-skin device from the chest of a volunteer before doing exercise (bottom) and after running one kilometer with a high moisture level (top), demonstrating the trivial effects of sweat on the device performance.

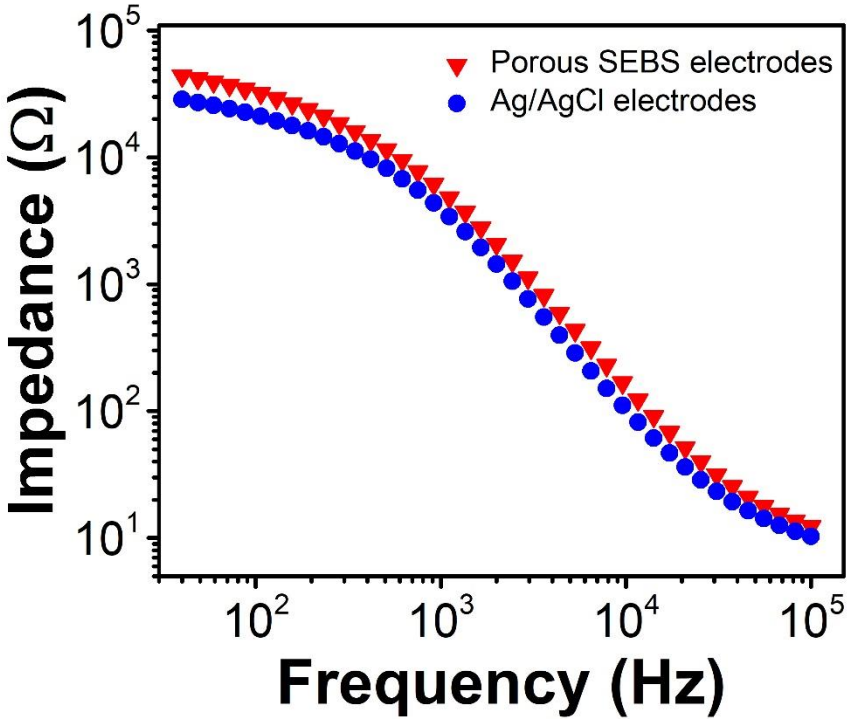

Fig. S20. Impedance of the skin/electrode interface. Commercial Ag/AgCl electrode is used as reference. A pair of our porous electrophysiological sensors and a pair of Ag/AgCl electrodes (Kendall™ 530 series, Cardinal Health) were laminated onto human forearm at the same location after cleaning the forearm with alcohol swabs. The size of our electrode and the Ag/AgCl electrode is 20 mm × 11 mm and the center-to-center distance is 15 mm.

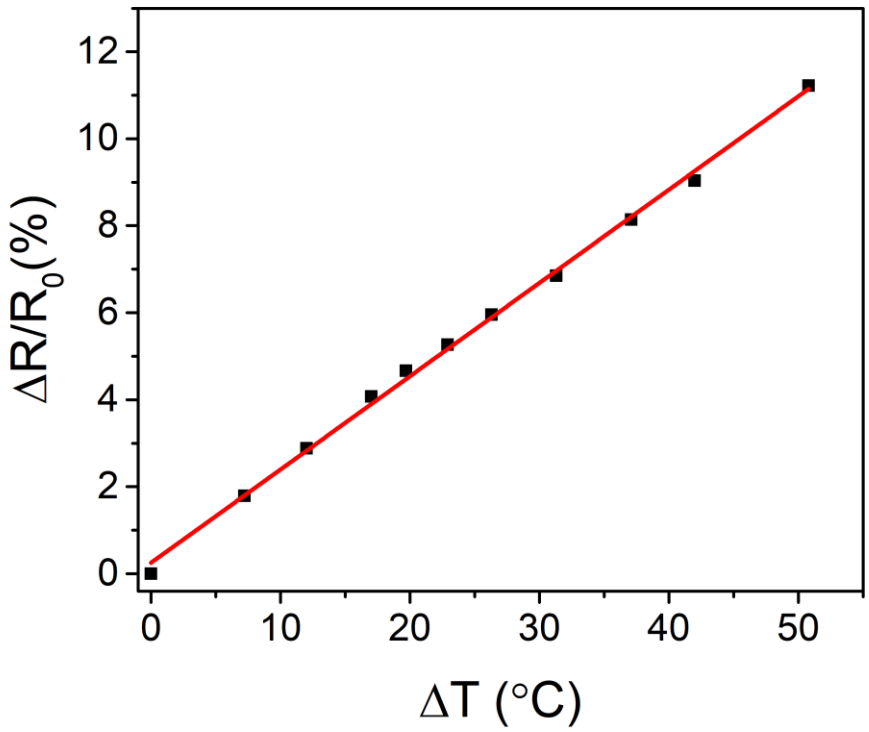

Fig. S21. Resistance variations of the Ag NWs-based on-skin temperature sensor as a function of temperature change. The temperature coefficient α, which is described as: $\frac{\Delta R}{R_0} = \alpha \cdot \Delta T$, is calculated to be 0.00214 °C^{-1}.

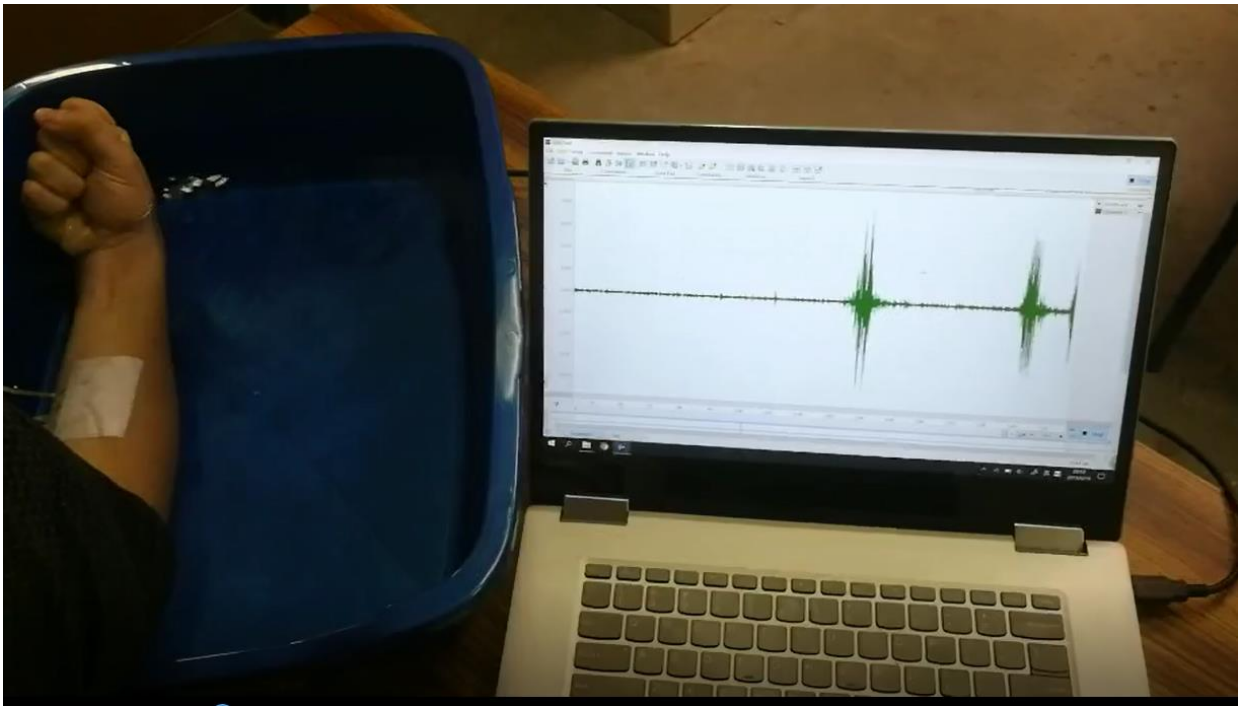

Fig. S22. EMGs recording in water, showing the uncompromised signal quality. Since the Ag NWs side is laminated onto human skin, the conformal contact between the porous SEBS substrate and skin allows the encapsulation of Ag NWs, blocking their direct contact with water, thus providing the waterproof capability of the Ag NWs even in water.

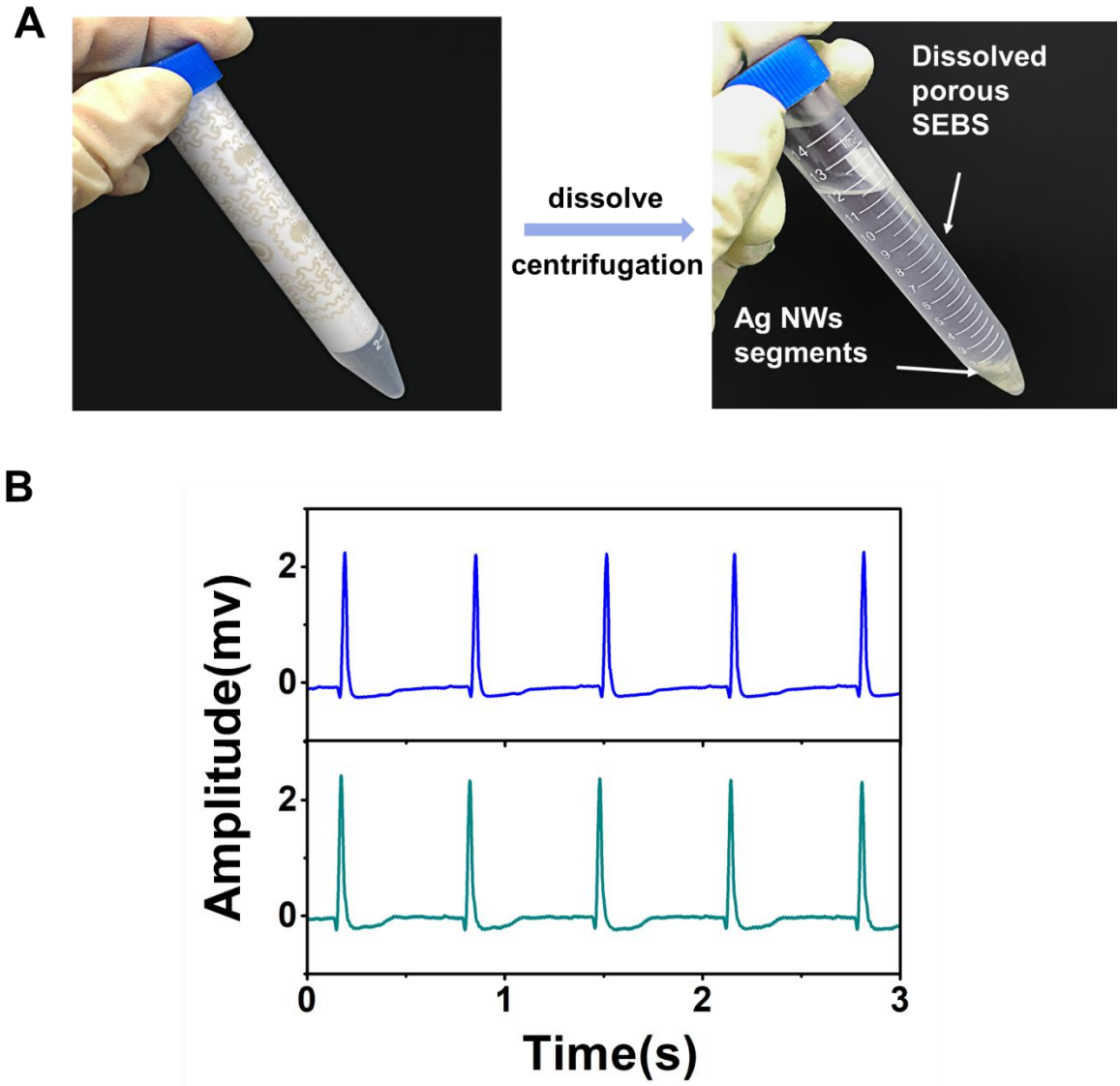

Fig. S23. Recyclability of porous SEBS composite. (A) The recycling process of the multifunctional on-skin electronic patch. **(B)** ECGs recorded using the on-skin device made of fresh SEBS and Ag NWs (bottom) and the one made of reused materials (top).

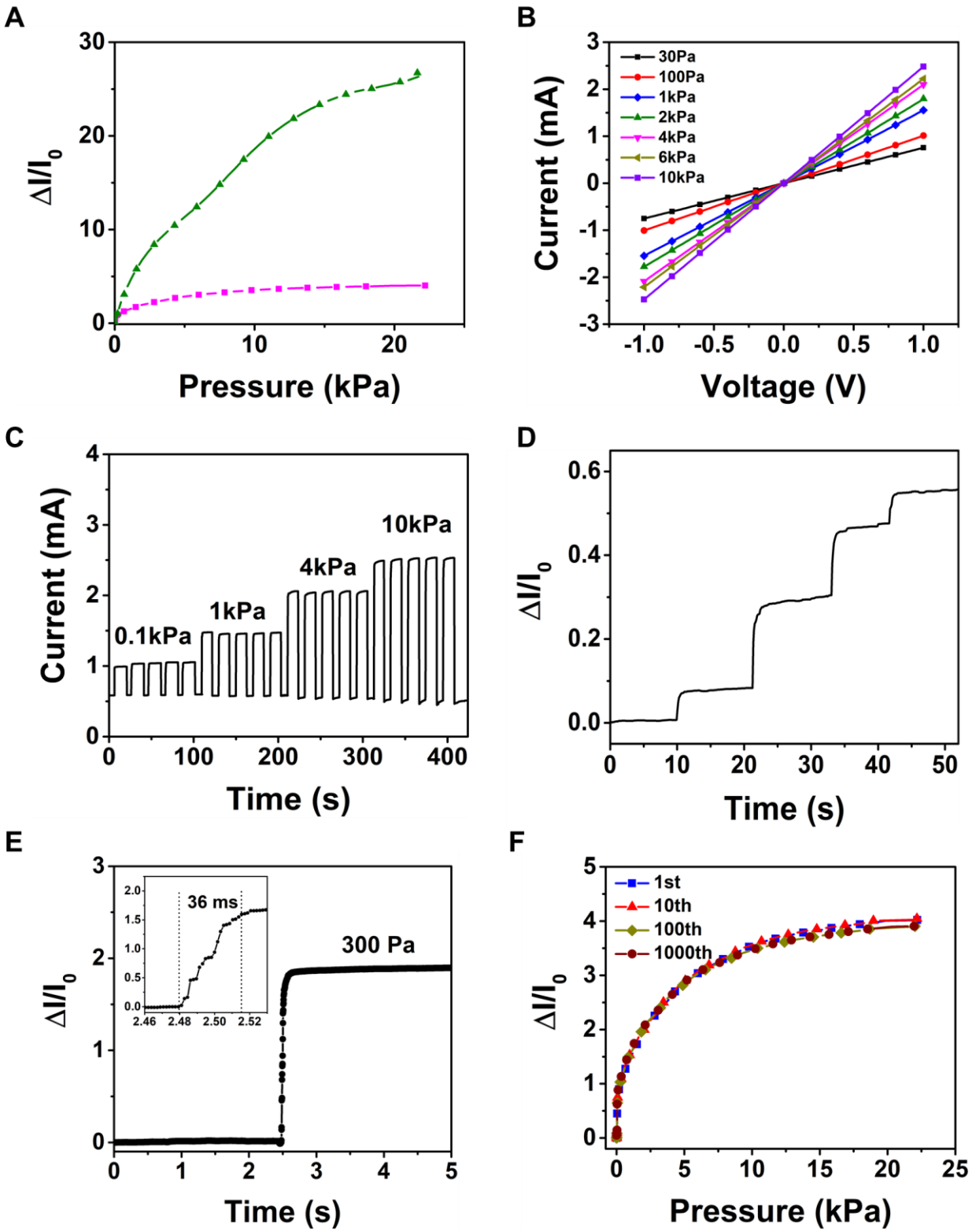

Fig. S24. Systematic characterizations of the assembled piezoresistive on-skin pressure sensor. (**A**) Relative change in the current of the pressure sensors, made of laser-induced porous graphene (LIG) with different sheet resistances (green: ~1MΩ/sq; red: ~10 kΩ/sq), under different pressures. As indicated in **A**, the pressure sensors, made of LIG with a higher sheet

resistance (green: ~1MΩ/sq), is more sensitive and can pick up a lot of noises during the on-skin measurement of pulse waveforms. Thus, in this research, LIG with the sheet resistance of ~10 kΩ/sq is adopted for the fabrication of the on-skin pressure sensor. (**B**) Current-voltage curves of the pressure sensor measured under various pressures ranging from 30 Pa to 10 kPa. (**C**) Dynamic responses of the pressure sensor under loading/unloading cycles for different pressures, showing a stable and immediate response. (**D**) Relative change in the current with the subtle increase of the pressures via stepwise addition of a 10 μl of water droplet. (**E**) Response time of the pressure sensor with a loading pressure of 300 Pa, indicating a quick response time of ~36 ms. (**F**) Relative change in the current of the pressure sensor under repetitive loading cycles, demonstrating the excellent repeatability.

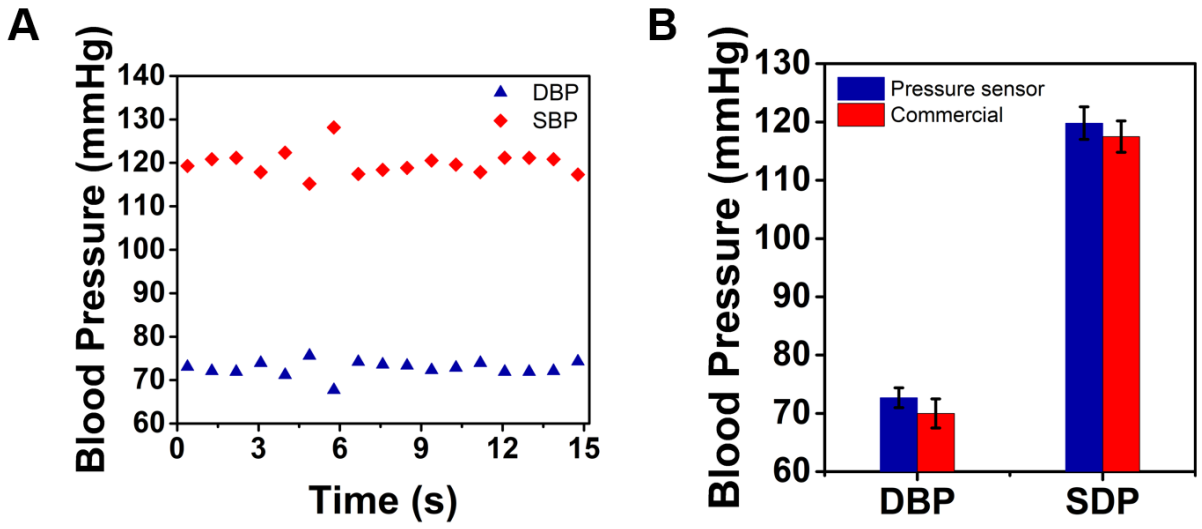

Fig. S25. Beat-to-beat blood pressure measurement. (**A**) Beat-to-beat systolic blood pressures (SDP) and diastolic blood pressures (DBP) extracted the pulse transmit time (PTT). (**B**) Comparisons of the DBP and SDP measured using the on-skin devices with the data measured from a commercial sphygmomanometer. The standard deviations of the blood pressures measured with the commercial sphygmomanometer are based on 6 readings.

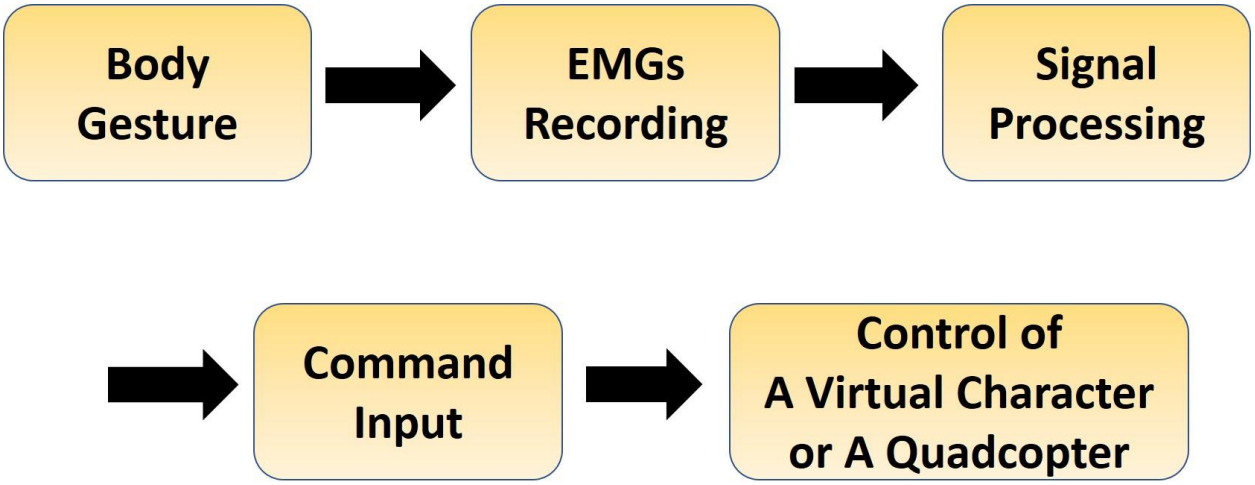

Fig. S26. The flow chart for the control of a virtual character or a quadcopter via real-time EMGs recording.

Table S1. Comparison of the passive-cooling performances of several functional materials, which are recently reported in literatures (1-4).

Materials		Cooling performance	References
Paint	P(VdF-HFP)	~6 °C	1
Wood	Delignified and densified wood	~4 °C	2
Textile	Nanoporous polyethylene	~2.7 °C	3
	NanoPE fabric	~2.3 °C	4
Elastic substrates of on-skin electronics	Multiscale porous SEBS	~6 °C	This work

Reference

1. Mandal, J. *et al*. Hierarchically porous polymer coatings for highly efficient passive daytime radiative cooling. *Science* **362**, 315-319 (2018).
2. Li, T. *et al*. A radiative cooling structural material. *Science* **364**, 760-763 (2019).
3. Hsu, P.C. *et al*. Radiative human body cooling by nanoporous polyethylene textile. *Science* **353**, 1019-1023 (2016).
4. Peng, Y. *et al*. Nanoporous polyethylene microfibres for large-scale radiative cooling fabric. *Nat. Sustain.* **1**, 105-112 (2018).